Time Spectral Method for Rotorcraft Flow

Nawee Butsuntorn* and Antony Jameson†
Stanford University, Stanford, California, 94305, U.S.A.

This paper proposes a fast and efficient way to simulate time-periodic unsteady three-dimensional rotorcraft flow for both Euler and Reynolds averaged Navier–Stokes equations. Based on the recently developed Time Spectral method, accurate results for hover and forward flight cases were achieved while gaining efficiency on the traditional dual time stepping scheme, and being simpler than the nonlinear frequency domain type solvers. Two new formulations for Vorticity Confinement for compressible flows were explored. The first formulation uses the local velocity magnitude to scale the confinement parameter and the second uses a helicity to determine the strength of the confinement term. The addition of the confinement term has no effect on the surface pressure distribution and negligible errors in the calculations of the coefficients of lift and drag.

I. Introduction

The accurate computation of helicopter rotor flows in both hover and forward flights continues to be a complex and challenging problem. Reliable prediction of helicopter performance is heavily dependent on the accurate prediction of the transonic flows on the advancing side of a helicopter rotor and proper resolution of blade–vortex and blade–wake interactions. To account for the former, a robust, fully compressible CFD solver is essential in computing the flow around rotor blades. Most compressible flow solvers, regardless of the numerical algorithms, introduce a certain amount of numerical dissipation, which can be intrinsic to the discretization or explicitly added to avoid numerical instability. This is a crucial issue because it may lead to erroneous dissipation of the wake or tip vortices and their subsequent spreading. Since the amount of dissipation is proportional to the mesh size, it is clear that there is a need for a method that captures the vortical structures in order to properly resolve a helicopter wake. Jameson[1–3] has developed high accuracy, low dissipation schemes for fixed-wing applications while Sheffer *et al.*[4] showed that the performance of these numerical schemes in the calculation of helicopter flows are robust and accurate. A lot of work has been done in the field of helicopter simulation in the past decades ranging from potential flow calculations (Caradonna & Isom,[5,6] Caradonna & Philippe[7]), Euler and Navier–Stokes (RANS) calculations (Agarwal & Deese,[8,9] Srinivasan *et al.*,[10,11] Allen,[12–16] Pomin & Wagner[17–19]), and hybrid methods (Hassan *et al.*,[20] Bhagwat *et al.*[21,22]), just to name a few. Most of the aforementioned computations employed some form of implicit time stepping scheme, mostly the dual time stepping scheme first introduced by Jameson.[23] While this has proved to be accurate for helicopter simulation, the time and computational resources required to compute a complete rotor in forward flight is very high, especially if the aeroelastic effects are to be considered.

During the course of the past few years, much effort has been placed at the Aerospace Computing Laboratory at Stanford University on the development of accurate and efficient methods for calculating flow which are inherently unsteady but periodic. Helicopter flows in forward flight, turbomachinery blades and wind turbine are constantly subjected to unsteady loads. For this class of problems, Gopinath & Jameson[24] have shown that the Time Spectral method is superior in terms of the accuracy and computational efficiency to the typical implicit dual time stepping scheme or the hybrid scheme proposed by Hsu & Jameson.[25] The Time Spectral method takes advantage of the periodic nature of the flow and is simpler than the typical nonlinear frequency domain type solver proposed by Hall *et al.*[26] and McMullen *et al.*[27–29] as it does not require the operations of Fourier transforms and inverse Fourier transforms.

*Doctoral Candidate, Department of Mechanical Engineering, Stanford University, AIAA Student Member.
†Thomas V. Jones Professor of Engineering, Department of Aeronautics & Astronautics, Stanford University, AIAA Member.

However, truly unsteady flow resolutions require prohibitive computational resources because of the number of mesh points required to resolve small vortical structures. Steinhoff;[30] Steinhoff & Underhill[31] proposed a method to capture vortices called Vorticity Confinement where the vortex is injected back into the vortex core. It was shown that this method is effective in treating concentrated vortical regions in coarse grids. The original Vorticity Confinement method was derived for incompressible Euler equations, so there are some discrepancies when used in the flow fields that are transonic, as in helicopter rotor in either hover or forward flights. Hu *et al.*;[32] Hu & Grossman;[33] Dadone *et al.*[34] introduced a new formulation of Vorticity Confinement for compressible flow. Nevertheless, all variations of the scheme require a confinement parameter ϵ, which is completely arbitrary and needs to be adjusted for each case. Fedkiw *et al.*;[35] Löhner & Yang;[36] Löhner *et al.*[37] made further attempts to define the parameter ϵ that dynamically varies for different parts of the flow field, although these attempts were made for incompressible Euler and Navier–Stokes equations.

This paper shows that simulation of rotorcraft flows can adhere to engineering accuracy without the need of massive computing resources or long turnaround time by utilizing the Time Spectral method in the flow solver while the method of Vorticity Confinement is also considered for future application in order to capture the traveling vortices in relatively coarse meshes.

II. Governing Equations and Discretization

Let p, ρ, E and H denote the pressure, density, total energy and total enthalpy of the fluid. The Cartesian coordinates and velocity components are denoted by x_1, x_2, x_3 and u_1, u_2, u_3 respectively. Einstein notation is used to simplify the presentation of the equations where the summation is implied with the repeated index.

Consider the flow equations without the body force in integral form:

$$\frac{\partial}{\partial t}\int_{\Omega} \vec{w}\,\mathrm{d}\mathcal{V} + \oint_{\partial\Omega} \vec{f_j}\cdot\vec{n}\,\mathrm{d}\mathcal{S} = 0 \tag{1}$$

where $\vec{w}$ is the state vector with the following components:

$$\vec{w} = \begin{bmatrix} \rho \\ \rho u_1 \\ \rho u_2 \\ \rho u_3 \\ \rho E \end{bmatrix}.$$

The flux $\vec{f_j}$ can be split into the convective and viscous components:

$$\vec{f_j} = \vec{f}_{j,c} - \vec{f}_{j,v} \tag{2}$$

where $\vec{f}_{j,c}$ is the convective flux and $\vec{f}_{j,v}$ is the viscous flux. Consider the control volume boundary that moves with the velocity $b_j = \frac{\partial x_j}{\partial t}$, the flux terms can now be written as

$$\vec{f}_{j,c} = \begin{bmatrix} \rho\,(u_j - b_j) \\ \rho u_1\,(u_j - b_j) + p\,\delta_{1j} \\ \rho u_2\,(u_j - b_j) + p\,\delta_{2j} \\ \rho u_3\,(u_j - b_j) + p\,\delta_{3j} \\ \rho E\,(u_j - b_j) + p\,u_j \end{bmatrix} \quad \text{and} \quad \vec{f}_{j,v} = \begin{bmatrix} 0 \\ \tau_{1j} \\ \tau_{2j} \\ \tau_{3j} \\ u_m\cdot\tau_{mj} - q_j \end{bmatrix} \tag{3}$$

where δ_{mj} is the Kronecker delta, q_j is the heat flux in the j direction and τ_{mj} is the stress tensor. Its components are given by

$$\tau_{jj} = 2\mu\frac{\partial u_j}{\partial x_j} + \lambda\left(\frac{\partial u_1}{\partial x_1} + \frac{\partial u_2}{\partial x_2} + \frac{\partial u_3}{\partial x_3}\right)$$

and

$$\tau_{mj} = \tau_{jm} = \mu\left(\frac{\partial u_j}{\partial x_m} + \frac{\partial u_m}{\partial x_j}\right)$$

where μ is the dynamic viscosity of the fluid and λ is the second coefficient of viscosity, which is equal to $-\frac{2}{3}\mu$. The dynamic viscosity can be modeled using Sutherland's law where μ is a function of temperature:

$$\mu = \frac{\left(1.458 \times 10^{-6}\right) T^{\frac{3}{2}}}{T + 110.4}, \qquad T = \frac{p}{(\gamma - 1)\rho}.$$

With the aid of Fourier's law of heat conduction, the heat flux q_j is defined as

$$q_j = -k \frac{\partial T}{\partial x_j},$$

where k is the thermal conductivity of the fluid, which is defined as

$$k = \frac{\gamma \mu}{\mathrm{Pr}}.$$

The values of the ratio of specific heats, γ, and Prandtl number are held constant at 1.4 and 0.725 respectively. The equation of state provides the closure for the governing equations. For an ideal gas

$$E = \frac{p}{(\gamma - 1)\rho)} + \frac{1}{2}\left(u_j u_j\right), \qquad H = E + \frac{p}{\rho}.$$

For Euler calculation, the term $\vec{f}_{j,v}$ in Eq. (2) is set to zero.

Using central differencing with an artificial dissipation scheme for spatial discretization, the flow equations in Eq. (1), can be written in semi-discrete form:

$$\mathcal{V} \frac{\mathrm{d}\vec{w}}{\mathrm{d}t} + R(\vec{w}) = 0. \tag{4}$$

II.A. RANS Equations

FOR high Reynolds number flow in which the flow becomes turbulent, the Reynolds averaged Navier–Stokes (RANS) equations are derived by ensemble time averaging. This results in nine additional unknowns termed the Reynolds stresses, $\frac{\partial}{\partial x_m}\left(\overline{u_j u_m}\right)$. However, these Reynolds stresses are symmetric, therefore there are only six unknowns. There are various types/levels of closures. There are zero-equation, one-equation and two-equation models, which are scalar models. Additionally there are Reynolds stress transport models, which are tensor models. In the simple closures, the total dynamic viscosity of the fluid can be calculated by the addition of the dynamic viscosity and the turbulent dynamic viscosity:

$$\mu_{\mathrm{total}} = \mu + \mu_t.$$

The total thermal conductivity now becomes

$$\begin{aligned} k_{\mathrm{total}} &= k + k_t \\ &= \gamma \left(\frac{\mu}{\mathrm{Pr}} + \frac{\mu_t}{\mathrm{Pr}_t} \right). \end{aligned}$$

where k_t is the thermal conductivity due to the effect of turbulence, μ_t is the turbulent dynamic viscosity of the fluid, and Pr_t is the turbulent Prandtl number, which is held constant at 0.9. The value of turbulent dynamic viscosity μ_t (or more commonly referred to as eddy viscosity, $\nu_t = \mu_t/\rho$) can be calculated by many different turbulence models. In the present work, Baldwin–Lomax[38] zero-equation turbulence model is used for the closure.

II.B. Steady State Hover Calculations

For the hover case, if one wishes to solve for the absolute velocities without physically rotating the computational grid, we can add a source term to the flow equations in Eq. (1). According to Holmes & Tong,[39] this results in

$$\int_\Omega \frac{\partial \vec{w}}{\partial t} \mathrm{d}\mathcal{V} + \oint_{\partial\Omega} \vec{f}_j \cdot \vec{n} \, \mathrm{d}\mathcal{S} = \int_\Omega \vec{T} \mathrm{d}\mathcal{V} \tag{5}$$

where $\vec{T}$ is defined as

$$\vec{T} = \begin{bmatrix} 0 \\ \rho\Omega u_3 \\ 0 \\ -\rho\Omega u_1 \\ 0 \end{bmatrix}$$

for a rotor that lies in the (x, z) plane with Ω as the angular velocity. With this formulation, the problem can now be solved as a steady-state hover problem.

The calculations presented in this paper for the hover cases were solved as steady state problems using the formulation presented in Eq. (5), unless stated otherwise.

III. Time Spectral Method

TAKING advantage of the periodic nature of the periodic unsteady problem, a Fourier representation in time can make it possible to achieve spectral accuracy. However, typical nonlinear frequency domain solvers require forward and backward Fourier transforms between the time and frequency domain for every time step. The Time Spectral method addresses this problem by utilizing the Fourier collocation matrix. As a result, the governing equations are now solved strictly in the time domain only.

Recall that for a real, periodic function, $f(x)$, defined on N equally spaced grid points, $x_j = j\Delta x$ where $j = 0, 1, 2, \ldots, N-1$. The discrete Fourier transform of f is

$$\hat{f}_k = \frac{1}{N} \sum_{j=0}^{N-1} f_j \mathrm{e}^{-\mathrm{i}kx_j}, \tag{6}$$

and its inverse transform is

$$f_j = \sum_{k=-\frac{N}{2}}^{\frac{N}{2}-1} \hat{f}_k \mathrm{e}^{\mathrm{i}kx_j}. \tag{7}$$

Then, the Fourier transform of the derivative approximation is computed by multiplying the Fourier transform of f by $\mathrm{i}k$

$$\widehat{Df_k} = \mathrm{i}k\hat{f}_k.$$

Therefore the spectral derivative of f at point j is

$$\left.\frac{\mathrm{d}f}{\mathrm{d}x}\right|_j = \sum_{k=-\frac{N}{2}+1}^{\frac{N}{2}-1} \widehat{Df_k} \mathrm{e}^{\mathrm{i}kx_j}.$$

Note that in the above representation, the period in space is 2π, and the Fourier coefficient of the derivative corresponding to the wave number $-N/2$ is set to zero to avoid complex derivatives.

If one wishes to have a compact representation of the spectral Fourier derivative operator in the physical space and not in the wave space, a physical (time) space operator for numerical differentiation can be derived for the governing equations as follows.

Using the definition from Eqs. (6) and (7), the discrete Fourier transform of the flow variables $\vec{w}$ for a time period T is

$$\widehat{\vec{w}}_k = \frac{1}{N} \sum_{n=0}^{N-1} \vec{w}^n \mathrm{e}^{-\mathrm{i}k\frac{2\pi}{T}n\Delta t},$$

and its inverse transform is

$$\vec{w}^n = \sum_{k=-\frac{N}{2}}^{\frac{N}{2}-1} \widehat{\vec{w}}_k \mathrm{e}^{\mathrm{i}k\frac{2\pi}{T}n\Delta t} \tag{8}$$

where $n\Delta t$ is the n-th time instance in the period T. The spectral derivative of Eq. (8) with respect to time at the n-th time stance is given by

$$D\vec{w}^n = \frac{2\pi}{T} \sum_{k=-\frac{N}{2}+1}^{\frac{N}{2}-1} \mathrm{i}k\, \widehat{\vec{w}}_k \mathrm{e}^{\mathrm{i}k\frac{2\pi}{T}n\Delta t}.$$

This summation involves the Fourier transform of $\vec{w}$ but it can be written as a matrix multiplication in the time domain as

$$D\vec{w}^n = \sum_{j=0}^{N-1} d_n^j \vec{w}^j$$

where

$$d_n^j = \begin{cases} \frac{2\pi}{T}\frac{1}{2}(-1)^{n-j}\cot\left\{\frac{\pi(n-j)}{N}\right\} & : \quad n \neq j \\ 0 & : \quad n = j \end{cases}.$$

This representation of the time derivative expresses the multiplication of a matrix (Canuto *et al.*, 2007)[40] with elements d_j^n and the vector $\vec{w}^j$.

Let $n - j = -m$, one can rewrite the time derivative as

$$D\vec{w}^n = \sum_{m=-\frac{N}{2}+1}^{\frac{N}{2}-1} d_m \vec{w}^{(n+m)}, \tag{9}$$

where d_m is now given by

$$d_m = \begin{cases} \frac{2\pi}{T}\frac{1}{2}(-1)^{m+1}\cot\left\{\frac{\pi m}{N}\right\} & : \quad m \neq 0 \\ 0 & : \quad m = 0 \end{cases}.$$

Substituting the spectral derivative of the flow variables in Eq. (9) into Eq. (4), the flow equations in semi-discrete form for the n-th time instance is

$$\mathcal{V}D\vec{w}^n + R(\vec{w}^n) = 0. \tag{10}$$

Introducing a pseudo time derivative term to Eq. (10), the equations can now be marched towards a periodic steady state using well known convergence acceleration techniques

$$\mathcal{V}\frac{\mathrm{d}\vec{w}^n}{\mathrm{d}\tau} + \mathcal{V}D\vec{w}^n + R(\vec{w}^n) = 0. \tag{11}$$

III.A. Numerical Methods

In order to solve Eq. (11) to the steady state as quickly as possible, the flow solver incorporated a number of convergence acceleration techniques; local time stepping, modified five stage Runge–Kutta time stepping scheme[41] and multigrid.[42,43] Three different artificial dissipation schemes were used; Jameson–Schmidt–Turkel[1] (JST), symmetric limited positive[2] (SLIP) and convective upwind and split pressure[3] (CUSP).

For the RANS calculations of the forward flight, Message Passing Interface (MPI) were used between blocks. All the meshes used in this work were generated internally by the flow solvers. In the case of forward flight calculations, domain decomposition was done automatically.

IV. Vorticity Confinement for Compressible Flow

Steinhoff;[30] Steinhoff & Underhill[31] introduced the concept of Vorticity Confinement in 1994 and have been refining the model over the past decade. The basic idea of this method is to add a forcing term to the incompressible momentum equations, resulting in

$$\frac{\partial\vec{u}}{\partial t} + (\vec{u}\cdot\nabla)\,\vec{u} = \frac{1}{\rho}\nabla p + \mu\nabla^2\vec{u} - \epsilon\vec{s} \tag{12}$$

where the simplest form of $\vec{s}$ is

$$\vec{s} = \hat{n} \times \vec{\omega},$$

and

$$\hat{n} = \frac{\nabla \vec{\eta}}{|\nabla \vec{\eta}|}.$$

The vorticity vector $\vec{\omega}$ given by

$$\vec{\omega} = \nabla \times \vec{u}.$$

The variable $\vec{\eta}$ is defined as

$$\vec{\eta} = |\vec{\omega}|\,.$$

The idea behind this formulation is that vorticity is convected in the direction determined by the gradients of the vorticity. The unit vector $\hat{n}$ points towards the core of the vortical region and the confinement term $\vec{s}$ convects the vorticity towards the centroid.

The big disadvantage of the above formulation is that it was formulated for incompressible Euler equations (the term μ in Eq. (12) is the numerical dissipation, not the dynamic viscosity of the fluid). Since the flow of a helicopter rotor in hover and forward flight almost always involves transonic flow, one needs a formulation of Vorticity Confinement suitable for compressible flow calculation. Hu *et al.*;[32] Hu & Grossman;[33] Dadone *et al.*[34] proposed a new formulation for compressible flow by introducing the body force per unit mass term to the governing equations. So the governing equations now take the form:

$$\int_{\Omega} \frac{\partial \vec{w}}{\partial t}\,\mathrm{d}\mathcal{V} + \oint_{\partial\Omega} \vec{f_j} \cdot \vec{n}\,\mathrm{d}\mathcal{S} = -\int_{\Omega} \epsilon \vec{s}\,\mathrm{d}\mathcal{V}.$$

The components of $\vec{s}$ in three dimensions are:

$$\vec{s} = \begin{bmatrix} 0 \\ \rho(\hat{n} \times \vec{\omega}) \cdot \vec{i} \\ \rho(\hat{n} \times \vec{\omega}) \cdot \vec{j} \\ \rho(\hat{n} \times \vec{\omega}) \cdot \vec{k} \\ \rho(\hat{n} \times \vec{\omega}) \cdot \vec{u} \end{bmatrix} = \begin{bmatrix} 0 \\ \rho\left(n_2\omega_3 - n_3\omega_2\right) \\ \rho\left(n_3\omega_1 - n_1\omega_3\right) \\ \rho\left(n_1\omega_2 - n_2\omega_1\right) \\ \rho\left\{\left(n_2\omega_3 - n_3\omega_2\right)u_1 + \left(n_3\omega_1 - n_1\omega_3\right)u_2 + \left(n_1\omega_2 - n_2\omega_1\right)u_3\right\} \end{bmatrix} \tag{13}$$

Although the above formulation shows a marked improvement over the original formulation, the parameter ϵ is still kept as a constant. This leaves for inconsistent results when the mesh variation is large. Fedkiw *et al.*[35] for the first time, included a linearly dependent parameter ϵ according to the mesh size h. Löhner & Yang;[36] Löhner *et al.*[37] further refined the definition of the parameter ϵ to include the length scale h as the characteristic length in the direction of $\nabla\,|\omega|$, as well as making ϵ dimensionless. The work of Fedkiw *et al.*;[35] Löhner & Yang;[36] Löhner *et al.*[37] however, is a treatment for incompressible Euler and Navier–Stokes equations, and in the work of Löhner & Yang;[36] Löhner *et al.*,[37] for unstructured meshes. Therefore one needs a better formulation for fully compressible flow on structured meshes.

Upon examining the definition of the confinement term, one can observe that the unit of ϵ is m/s. Robinson[44] proposed an interesting idea where the helicity was calculated in his formulation by factoring out $|\vec{\omega}|$, and ϵ was scaled with the velocity magnitude. Although the formulation provided by Robinson[44] is an improvement over the previous work in some ways, it does not have the confinement term for the total energy equation and it still fails to take into account the length scale in the flow field as in Löhner & Yang;[36] Löhner *et al.*[37] Therefore, combining the work of Robinson;[44] Löhner & Yang;[36] Löhner *et al.*;[37] Hu *et al.*;[32] Hu & Grossman;[33] Dadone *et al.*,[34] two new formulations are possible. In the first formulation, the confinement parameter ϵ is scaled with the velocity magnitude $|\vec{u}|$, thus making ϵ dimensionless. The confinement term in the momentum equations can now be written as

$$\vec{s} = \rho\,|\vec{u}|\,(\hat{n} \times \vec{\omega})\,. \tag{14}$$

Using the same formulation for the confinement term in the total energy equation as in Eq. (13), Eq. (14) now takes the form:

$$\vec{s} = \rho \left| \vec{u} \right| \begin{bmatrix} 0 \\ (\hat{n} \times \vec{\omega}) \cdot \vec{i} \\ (\hat{n} \times \vec{\omega}) \cdot \vec{j} \\ (\hat{n} \times \vec{\omega}) \cdot \vec{k} \\ (\hat{n} \times \vec{\omega}) \cdot \vec{u} \end{bmatrix}. \tag{15}$$

Additionally, by factoring out $|\vec{\omega}|$ from Eq. (14) and form a dot product between the local velocity vector and the vorticity $\vec{\omega}$, the second formulation for the momentum equations can now be written as

$$\vec{s} = \rho \left| \vec{u} \cdot \vec{\omega} \right| \left(\hat{n} \times \frac{\vec{\omega}}{|\vec{\omega}|} \right). \tag{16}$$

Similarly, with the addition of the confinement term in the total energy equation, Eq. (16) now becomes

$$\vec{s} = \rho \left| \vec{u} \cdot \vec{\omega} \right| \begin{bmatrix} 0 \\ \left(\hat{n} \times \frac{\vec{\omega}}{|\vec{\omega}|} \right) \cdot \vec{i} \\ \left(\hat{n} \times \frac{\vec{\omega}}{|\vec{\omega}|} \right) \cdot \vec{j} \\ \left(\hat{n} \times \frac{\vec{\omega}}{|\vec{\omega}|} \right) \cdot \vec{k} \\ \left(\hat{n} \times \frac{\vec{\omega}}{|\vec{\omega}|} \right) \cdot \vec{u} \end{bmatrix} \tag{17}$$

where $|\vec{u} \cdot \vec{\omega}|$ in Eqs. (16) and (17) represents a helicity. This formulation looks attractive for rotorcraft simulation because the vortices generated from the blades are aligned with the velocity vector. Additionally, one should also account for the length scale of the local mesh cell in finite volume calculation on structured meshes. One of the simplest approaches is to scale the constant ϵ according to the cubed root of the ratio of the local cell volume and the averaged cell volume in the computational domain:

$$\epsilon \propto \left(\frac{\mathcal{V}}{\mathcal{V}_{\text{average}}} \right)^{1/3}.$$

So now ϵ varies with the length scale of each mesh cell. With this simple formulation substituted into Eq. (15), the resulting components of the confinement term for compressible flow with the body force term in the total energy equation are

$$\vec{s} = \rho \left| \vec{u} \right| \left(\frac{\mathcal{V}}{\mathcal{V}_{\text{averaged}}} \right)^{1/3} \cdot \begin{bmatrix} 0 \\ (\hat{n} \times \vec{\omega}) \cdot \vec{i} \\ (\hat{n} \times \vec{\omega}) \cdot \vec{j} \\ (\hat{n} \times \vec{\omega}) \cdot \vec{k} \\ (\hat{n} \times \vec{\omega}) \cdot \vec{u} \end{bmatrix} \tag{18}$$

where $\vec{u}$ is the local velocity vector and ϵ is now dimensionless.

On the other hand, if one wants to calculates the helicity directly as in Eq. (17) but with the body force term in the total energy equation, the resulting components of the vector $\vec{s}$ are

$$\vec{s} = \rho \left| \vec{u} \cdot \vec{\omega} \right| \left(\frac{\mathcal{V}}{\mathcal{V}_{\text{averaged}}} \right)^{1/3} \cdot \begin{bmatrix} 0 \\ \left(\hat{n} \times \frac{\vec{\omega}}{|\vec{\omega}|} \right) \cdot \vec{i} \\ \left(\hat{n} \times \frac{\vec{\omega}}{|\vec{\omega}|} \right) \cdot \vec{j} \\ \left(\hat{n} \times \frac{\vec{\omega}}{|\vec{\omega}|} \right) \cdot \vec{k} \\ \left(\hat{n} \times \frac{\vec{\omega}}{|\vec{\omega}|} \right) \cdot \vec{u} \end{bmatrix}. \tag{19}$$

The application of this last formulation depends on the type of flow. If the helical structure is normal to the free steam velocity (e.g. the vortical structure of a tornado is normal to the direction of its velocity), then the confinement term will become ineffective as $|\vec{u}\cdot\vec{\omega}|$ will tend to zero.

In finite volume calculations, especially the RANS calculations, where the difference between the smallest and largest cell volumes are very large, the ratio between $\mathcal{V}$ and $\mathcal{V}_{\text{averaged}}$ in most regions in the domain essentially becomes zero. In the case of the calculations on a NACA 0012 wing presented in section VII, the smallest cell volume in the domain is in the order of $\mathcal{O}(10^{-6})$ while the largest cell volume in the domain is in the order of $\mathcal{O}(10^{2})$. In order to apply the new formulations more effectively, one can use the log scale for the scaling parameter. Equations (18) and (19) become

$$\vec{s} = |\vec{u}| \left[1 + \log_{10}\left(1 + \frac{\mathcal{V}}{\mathcal{V}_{\text{averaged}}}\right)^{1/3}\right] \begin{bmatrix} 0 \\ \rho(\hat{n}\times\vec{\omega})\cdot\vec{i} \\ \rho(\hat{n}\times\vec{\omega})\cdot\vec{j} \\ \rho(\hat{n}\times\vec{\omega})\cdot\vec{k} \\ \rho(\hat{n}\times\vec{\omega})\cdot\vec{u} \end{bmatrix} \tag{20}$$

and

$$\vec{s} = |\vec{u}\cdot\vec{\omega}| \left[1 + \log_{10}\left(1 + \frac{\mathcal{V}}{\mathcal{V}_{\text{averaged}}}\right)^{1/3}\right] \begin{bmatrix} 0 \\ \rho\left(\hat{n}\times\frac{\vec{\omega}}{|\vec{\omega}|}\right)\cdot\vec{i} \\ \rho\left(\hat{n}\times\frac{\vec{\omega}}{|\vec{\omega}|}\right)\cdot\vec{j} \\ \rho\left(\hat{n}\times\frac{\vec{\omega}}{|\vec{\omega}|}\right)\cdot\vec{k} \\ \rho\left(\hat{n}\times\frac{\vec{\omega}}{|\vec{\omega}|}\right)\cdot\vec{u} \end{bmatrix}. \tag{21}$$

respectively.

V. Hover Simulations Results

This section presents numerical results from three-dimensional Euler calculations for three hover cases. Calculations were performed modeling an untapered, untwisted two-bladed rotor based on NACA 0012 section with the aspect ratio of 6. Experimental results for this rotor at different Mach numbers and collective pitch angles are from Caradonna & Tung.[45]

Figure 1 shows the topology of the O–H mesh for a single sector of a two-bladed rotor with the NACA 0012 section. The blade has finer mesh distribution near the tip, and is a single block mesh internally generated by the flow solver. All the hover calculations used only one block of the blade sector.

It is commonly assumed that the rotor rotation direction is in the counter-clockwise direction when viewed from above. However, the work presented in this paper, the rotor rotation direction is in the clockwise direction. At the periodic boundaries, the conservative variables in the halo cells in the downstream boundary are evaluated using the following transformation:

$$\begin{bmatrix} \rho \\ \rho u_1 \\ \rho u_2 \\ \rho u_3 \\ \rho E \end{bmatrix}_{\text{downstream, } JE} = \begin{bmatrix} 1 & 0 & 0 & 0 & 0 \\ 1 & \cos\left(\frac{2\pi}{N}\right) & 0 & \sin\left(\frac{2\pi}{N}\right) & 0 \\ 0 & 0 & 1 & 0 & 0 \\ 1 & -\sin\left(\frac{2\pi}{N}\right) & 0 & \cos\left(\frac{2\pi}{N}\right) & 0 \\ 0 & 0 & 0 & 1 & 0 \end{bmatrix} \cdot \begin{bmatrix} \rho \\ \rho u_1 \\ \rho u_2 \\ \rho u_3 \\ \rho E \end{bmatrix}_{\text{upstream, } JL} \tag{22}$$

where JE denotes the first halo cells and JL denotes the inner cells at the boundary in the y direction.

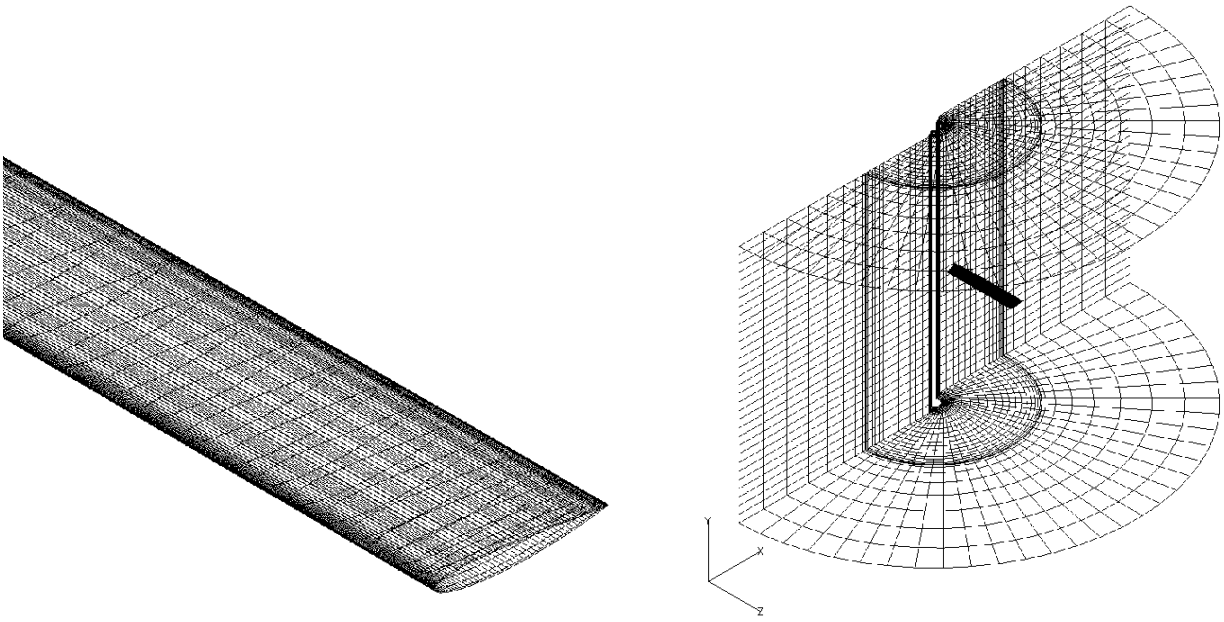

(a) Blade tip (b) Computational domain

Figure 1. View of the O–H mesh used in the nonlifting Euler calculation

Similarly, the transformation matrix for the upstream boundary is

$$\begin{bmatrix} \rho \\ \rho u_1 \\ \rho u_2 \\ \rho u_3 \\ \rho E \end{bmatrix}_{\text{upstream, } JE} = \begin{bmatrix} 1 & 0 & 0 & 0 & 0 \\ 1 & \cos\left(\frac{2\pi}{N}\right) & 0 & -\sin\left(\frac{2\pi}{N}\right) & 0 \\ 0 & 0 & 1 & 0 & 0 \\ 1 & \sin\left(\frac{2\pi}{N}\right) & 0 & \cos\left(\frac{2\pi}{N}\right) & 0 \\ 0 & 0 & 0 & 1 & 0 \end{bmatrix} \cdot \begin{bmatrix} \rho \\ \rho u_1 \\ \rho u_2 \\ \rho u_3 \\ \rho E \end{bmatrix}_{\text{downstream, } JL} . \tag{23}$$

V.A. Nonlifting Rotor

To verify the general algorithm of the flow solver, a nonlifting case was tested. This is a good case for testing the flow solver in the absence of downwash effects and the blade–vortex interaction. For this nonlifting case, the tip Mach number was 0.52, the collective pitch was zero degree with the angular velocity, Ω, of 1500 RPM. The tip Mach number is defined as

$$\mathrm{M}_{\text{tip}} = \frac{\Omega R}{a_0}$$

where R is the radius of the rotor and a_0 is the reference speed of sound.

V.A.1. Boundary Conditions for Nonlifting Rotor

Riemann invariants for one-dimensional flow normal to the boundary was applied for the three far-field boundaries (top, bottom and the far-field in the spanwise direction). Solid body boundary condition was used at the rotor hub. Periodic boundary conditions described in Eqs. (22) and (23) were used at the remaining two boundaries.

V.A.2. Nonlifting Rotor Results

The Euler calculation was performed on $128 \times 48 \times 32$ cells with 128 cells in the chordwise direction, 48 cells in the direction normal to the blade and 32 cells in the spanwise direction. The computed results at different

span stations are shown in Fig. 2, which show excellent agreement with the experimental data.

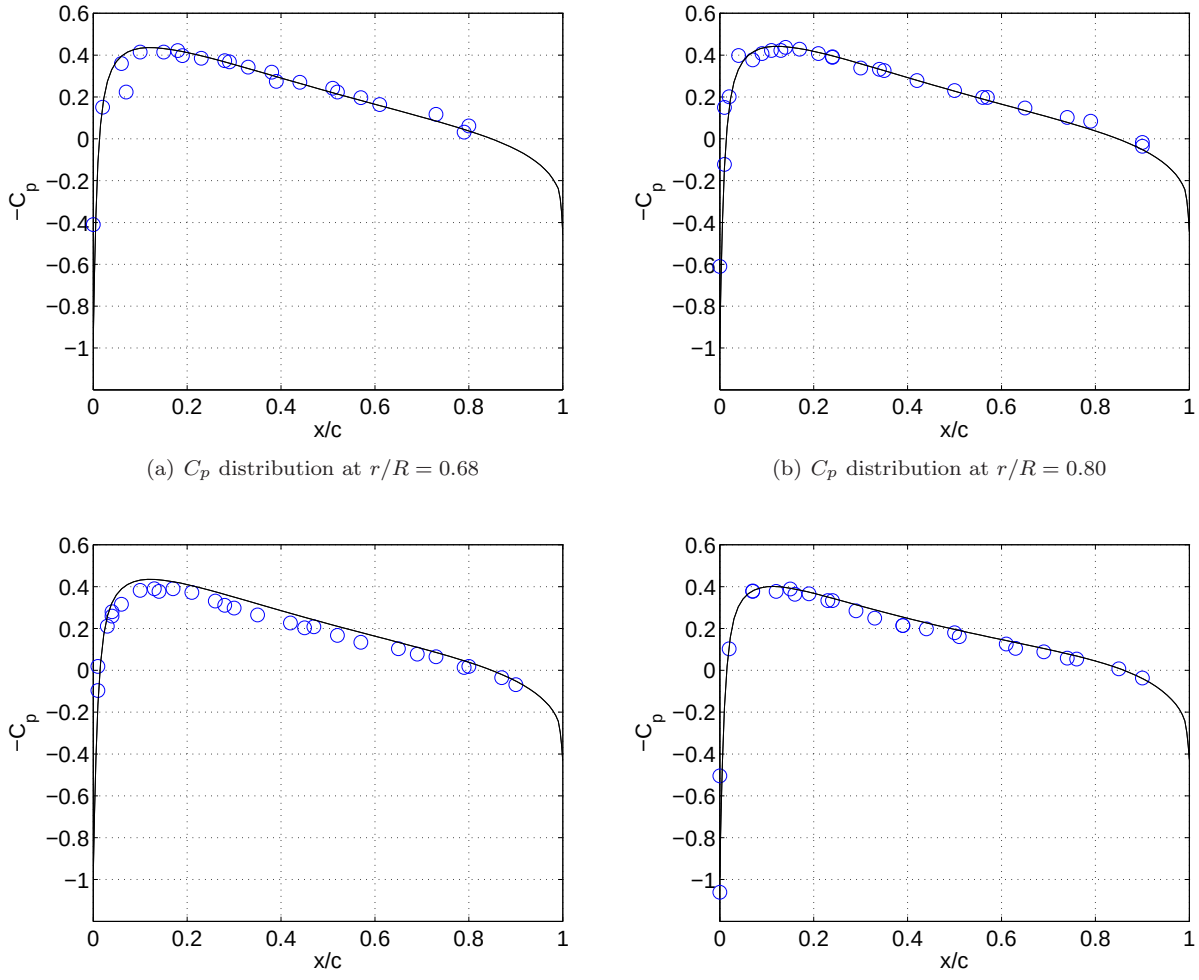

(a) C_p distribution at $r/R = 0.68$

(b) C_p distribution at $r/R = 0.80$

(c) C_p distribution at $r/R = 0.89$

(d) C_p distribution at $r/R = 0.96$

Figure 2. Coefficient of pressure distribution on a nonlifting rotor in hover using the JST dissipation scheme: M_{tip} = .52, $\theta_c = 0°$, ∘ denotes the experimental values, and — represents the computed result.

V.B. Lifting Rotor

Typically, when one uses Riemann invariants for far-field boundary conditions, the velocities tend to vanish outside the computational domain. While this assumption is acceptable for nonlifting rotor, it does not make physical sense for lifting rotor cases. The above assumption implies that the flow circulates inside the computational domain, while in reality, the rotor disk continuously draws the fluid from outside the computational box. To remedy this inconsistency, Srinivasan *et al.*[10] modeled this process as a sink in the downwash boundary. Using one-dimensional momentum theory, the mass flow requirements can be satisfied with better agreement compared to the experimental results.

V.B.1. Boundary Conditions

Riemann invariants for one-dimensional flow normal to the boundary was used for the two far-field boundaries (top and the far-field in the spanwise direction). At the rotor hub, a solid body boundary condition was used. One-dimensional momentum theory was applied at the bottom boundary to account for the downwash within the disk area that had the radius of $\sqrt{2}R_\infty = R$, where R is the radius of the rotor and R_∞ is

the radius of the rotor wake. Outside this area, the Riemann invariants boundary condition was applied. Periodic boundary conditions described in Eqs. (22) and (23) were used at the remaining two boundaries. The downwash velocity can be found by the following relation:[46]

$$v_w = \sqrt{2C_T}\,\Omega R$$

where v_w is the downwash velocity pointing downward, C_T is the coefficient of thrust, Ω is the angular velocity, and R is the radius of the rotor. A known coefficient of thrust is needed for this boundary condition; the values were taken from Ref. 45 for the two lifting rotor cases.

V.B.2. Lifting Rotor Results

Two lifting cases were performed; a subsonic and a transonic lifting rotor. Two artificial dissipation schemes were used in the Euler calculations; the JST and SLIP schemes. In the first lifting case, the tip Mach number was 0.439, the collective pitch was 8 degrees and the angular velocity was 1250 RPM. This was a subsonic case.

The computed results from the Euler calculations using both the JST and SLIP dissipation schemes are shown in Fig. 3. Since this case did not require the flow solver to capture any discontinuity, the results from both schemes look identical and are in prefect agreement with the experimental data.

The second lifting rotor case had the tip Mach number of 0.877 with the collective pitch of 8 degrees. The angular velocity of this case was 2500 RPM. This case required the flow solver to capture the discontinuity near the blade tip. The computed results from the Euler calculations with the JST and SLIP dissipation schemes are shown in Fig. 4.

Some differences can be found in the second lifting rotor case. In the transonic regime, the shock strength captured with the SLIP dissipation scheme was sharper. This was expected because there is more numerical dissipation built into the JST dissipation scheme. The shock location computed by both schemes occurred later than the location recorded in the experiment. Note that the "Zierep singularity" is present in the result computed with the SLIP dissipation scheme. Figure 5 shows the pressure coefficient distribution of the same lifting case. However, in this calculation, the entire two-bladed rotor was used for the simulation, with the two blades exchanging information that contained the conservative variables, halo grid points and mesh velocity at every time step at the common boundaries. The calculation used four time instances ($N = 4$) with the JST and CUSP dissipation schemes. The averaged residual reduced to almost four orders of magnitude in 250 multigrid cycles. The calculation was performed on four dual-core processors with the clock speed of 3.0 GHz and the total simulation time was 13 minutes. One notable aspect about this case was that the boundary condition at the bottom boundary was the standard Riemann invariants, not the one-dimensional momentum theory mentioned earlier in this section. As the result shows, it worked surprising very well for this particular case.

VI. Forward Flight Simulations Results

In forward flight regime, a component of free stream velocity U_0 adds or subtracts from the rotational velocity at each part of the blade. So the tip velocity U_{tip} now becomes

$$U_{\text{tip}} = \Omega R + U_0 \sin\psi$$

where ψ is the azimuthal angle of the blade. ψ is defined as zero in the downstream direction of the rotor. This angle is measured from downstream to the blade span axis.

Although the rotor blade is normally twisted along its length (linear twist), the blades in the current work are rigid and do not account for aeroelastic effects. Results are compared to the wind tunnel experiment of a model helicopter rotor in forward flight by Caradonna *et al.*[47] The blades were 7 feet in diameter and 6 inches in chord with an untapered, untwisted NACA 0012 profile.

VI.A. Mesh

The mesh for the forward flight calculations is an O–H type mesh similar to the mesh used in section V but forward flight calculation requires computation of the entire rotor, rather than just one section of the rotor

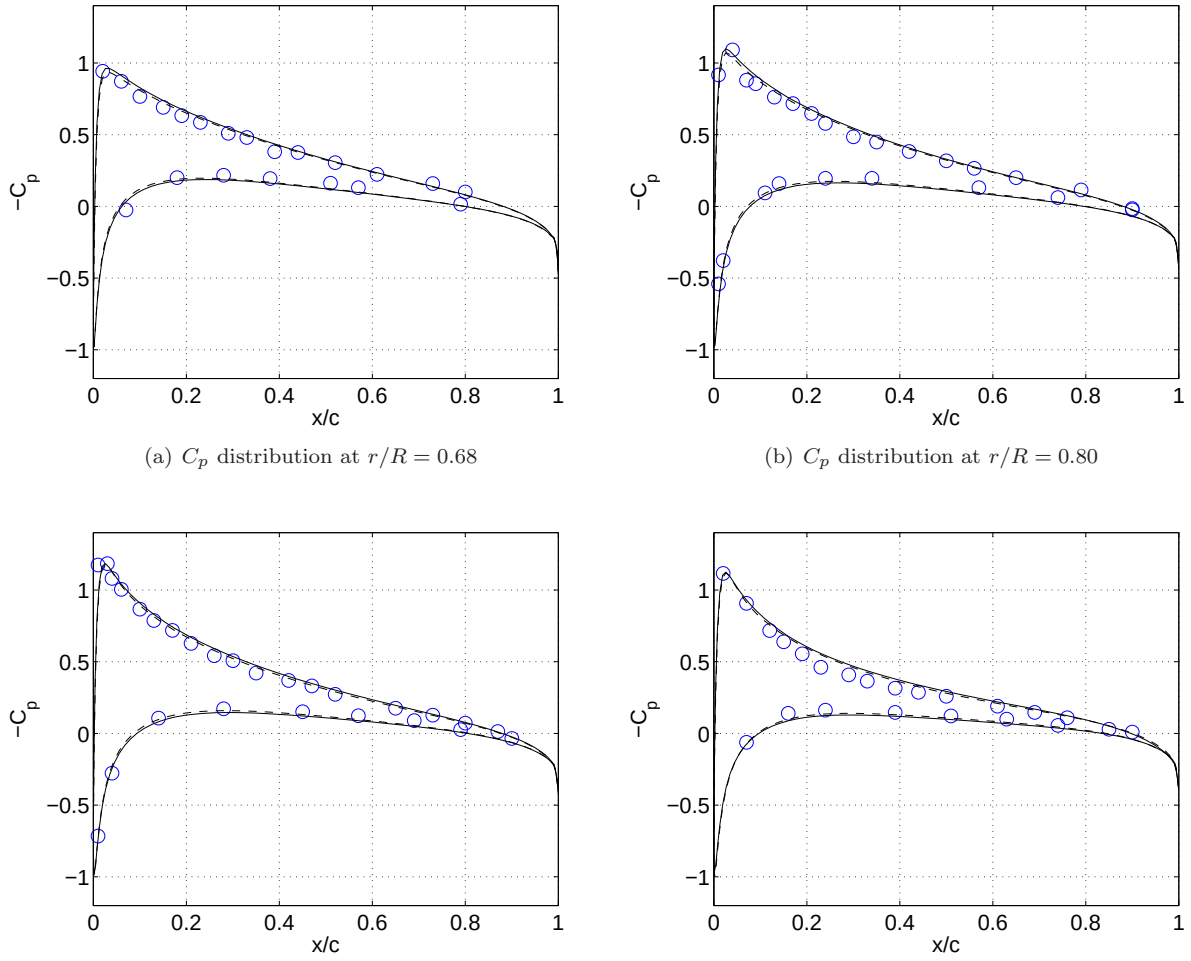

(a) C_p distribution at $r/R = 0.68$

(b) C_p distribution at $r/R = 0.80$

(c) C_p distribution at $r/R = 0.89$

(d) C_p distribution at $r/R = 0.96$

Figure 3. Coefficient of pressure distribution on a lifting rotor in hover: $M_{tip} = 0.439$, $\theta_c = 8°$, ∘ denotes the experimental values of C_p, — denotes the computed result using the JST dissipation scheme, and − − denotes the computed result using the SLIP dissipation scheme.

since periodic boundary conditions can no longer be used. Figure 6 shows the mesh of the rotor for forward flight calculation.

VI.B. Boundary Conditions

At the rotor hub, a solid body boundary (flow tangency for Euler calculation and no slip for RANS calculation) condition was used. Reimann invariants boundary condition was also tested but the overall result was insensitive to the boundary condition at this boundary.

At the far-field, the boundary condition was constructed using one-dimensional Reimann invariants for both the upper and lower boundaries. Since the calculations were for a nonlifting rotor in forward flight, there was no special treatment for the lower boundary as in the lifting hover case. The halo cells at the side boundaries containing both the values of the flow variables, mesh geometry and mesh velocities were exchanged between the blades at every time step.

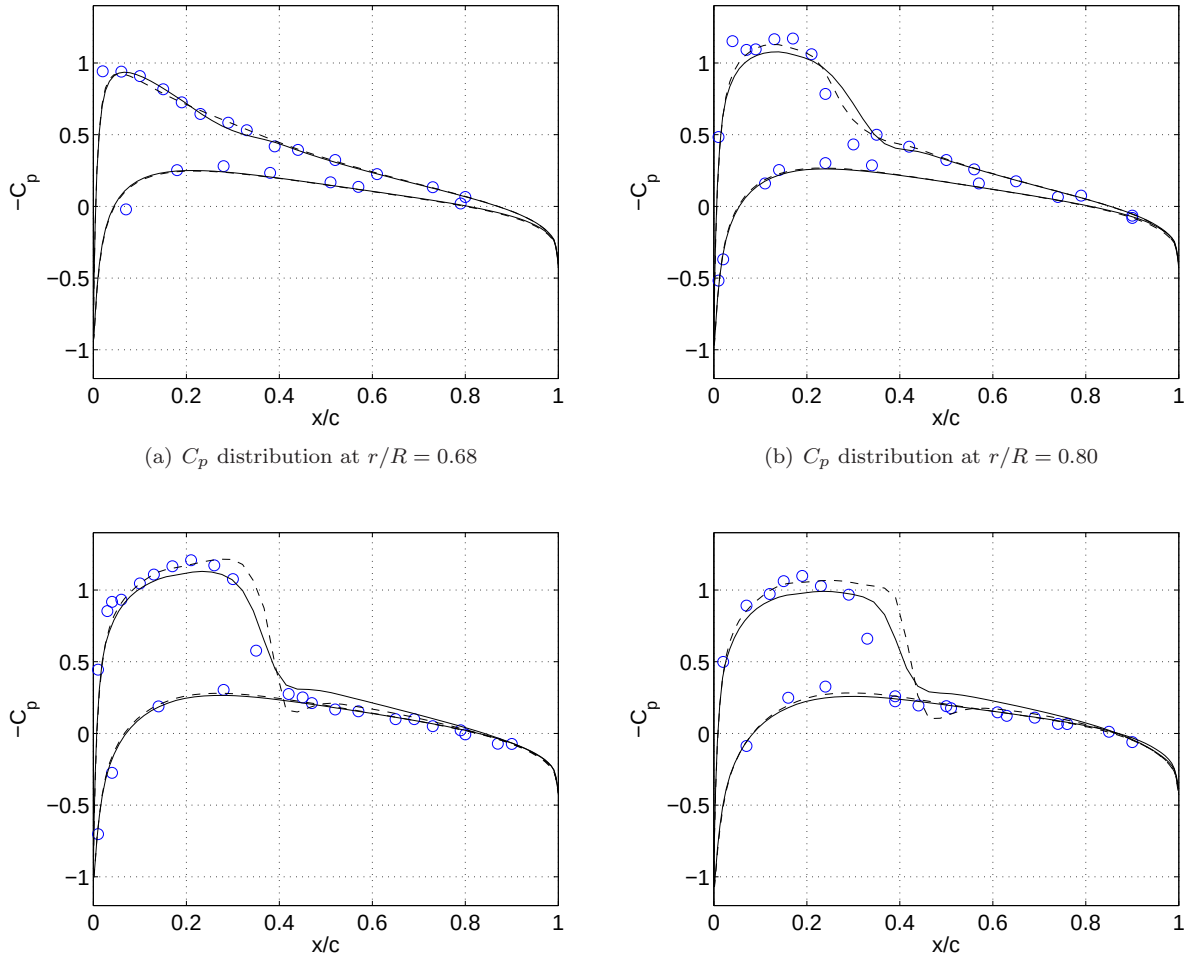

(a) C_p distribution at $r/R = 0.68$

(b) C_p distribution at $r/R = 0.80$

(c) C_p distribution at $r/R = 0.89$

(d) C_p distribution at $r/R = 0.96$

Figure 4. Coefficient of pressure distribution on a lifting rotor in hover: $M_{tip} = 0.877$, $\theta_c = 8°$, ∘ denotes the experimental values of C_p, — denotes the computed result using the JST dissipation scheme, and − − denotes the computed result using the SLIP dissipation scheme.

VI.C. Nonlifting Rotor in Forward Flight Results

The aspect ratio of the blades was 7. The tip Mach number was 0.8 with the reference Reynolds number of 2.89×10^6. The advance ratio was $\mu = 0.2$, which corresponded to a Mach number in the unperturbed flow of $M_0 = 0.16$.

For the Euler calculations, the number of cells per blade was $128 \times 48 \times 32$ with 16 cells distributed along the blade while $192 \times 64 \times 48$ cells were used for the RANS calculations with 32 cells distributed along each blade. All the calculations were performed with twelve time instances ($N = 12$), or five harmonics.

Figure 7 shows the variation of the local coefficient of pressure at the span location $r/R = 0.893$ for six different azimuthal angles. The results were from the Euler calculations with the JST and CUSP dissipation schemes. The agreement between the computed results and the experimental data was very good. The shock captured using the CUSP dissipation scheme was sharper and stronger, and is most obvious at the azimuthal angle $\psi = 120°$. The shock location calculated with both artificial dissipation schemes was almost the same, and this occurred earlier than the shock location recorded in the experiment. The Euler calculations took 300 multigrid cycles, by which time, the averaged residual was reduced by more than four orders of magnitude.

Figure 8 shows the result of the RANS calculations with the JST and CUSP dissipation schemes. Similarly, the calculations show excellent agreement with the experimental data. The result from the CUSP

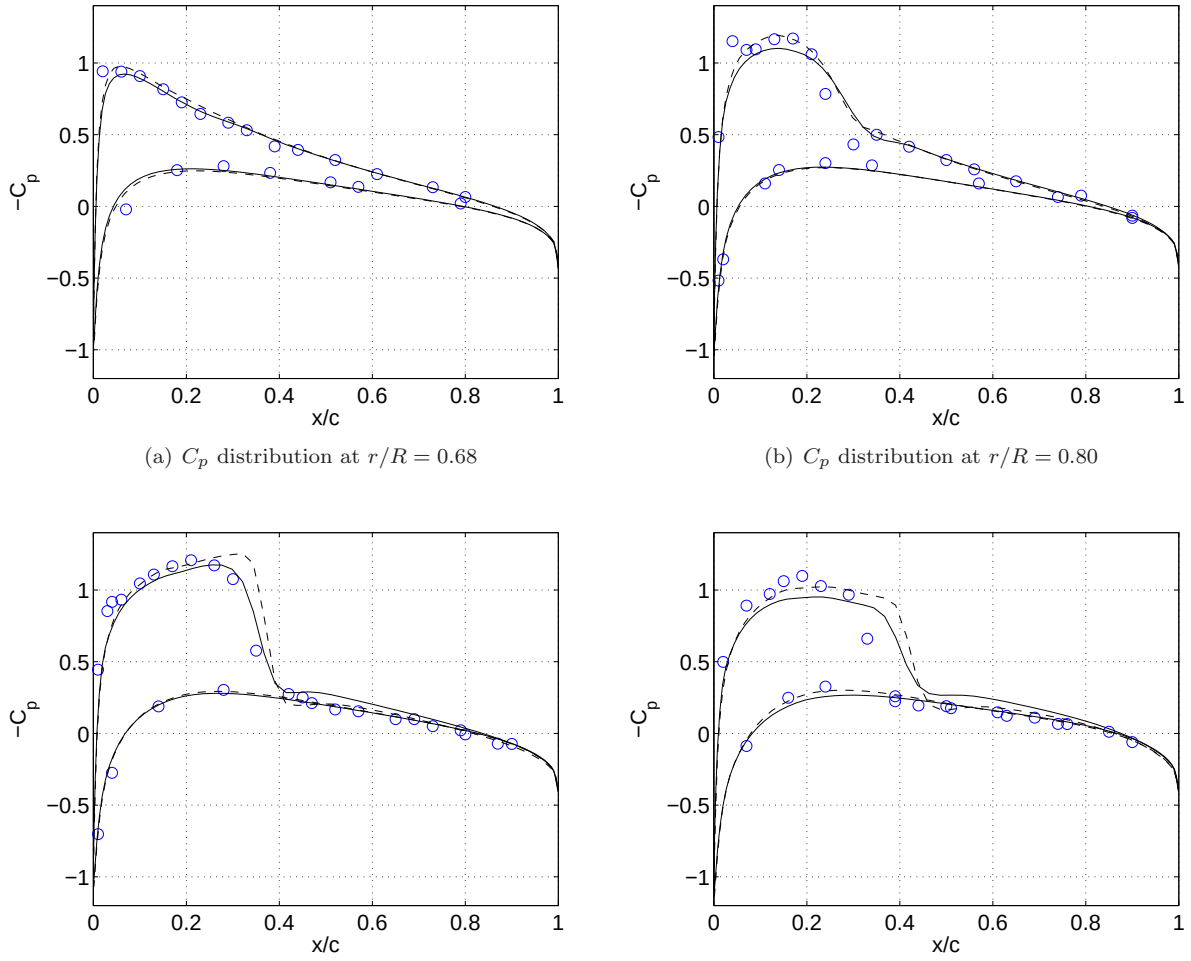

(a) C_p distribution at $r/R = 0.68$

(b) C_p distribution at $r/R = 0.80$

(c) C_p distribution at $r/R = 0.89$

(d) C_p distribution at $r/R = 0.96$

Figure 5. Coefficient of pressure distribution on a lifting rotor in hover (full rotor calculation): $M_{tip} = 0.877$, $\theta_c = 8°$, ∘ denotes the experimental values of C_p, — denotes the computed result using the JST dissipation scheme, and − − denotes the computed result using the CUSP dissipation scheme.

scheme showed slightly weaker shock in this calculation than in the corresponding Euler calculations. This was expected because of the viscous effects. The RANS computations with twelve time instances were run on four dual-core processors with the clock speed of 3.0 GHz. The total simulation time including mesh generation, which was built into the flow solver, was five hours for 500 multigrid cycles with three orders of magnitude reduction in the averaged residual.

VI.D. Accuracy Tests

As an accuracy test of the Time Spectral method, the forward flight case was simulated with only four time instances ($N = 4$). Results from Euler calculations at the azimuthal angles $\psi = 90°$ and $\psi = 180°$ are shown in Fig. 9. One can observe that even with a small number of time instances, as few as only four, the results still show excellent agreement with the experimental data. This shows that the Time Spectral method is indeed, a highly accurate scheme while avoids being computationally expensive.

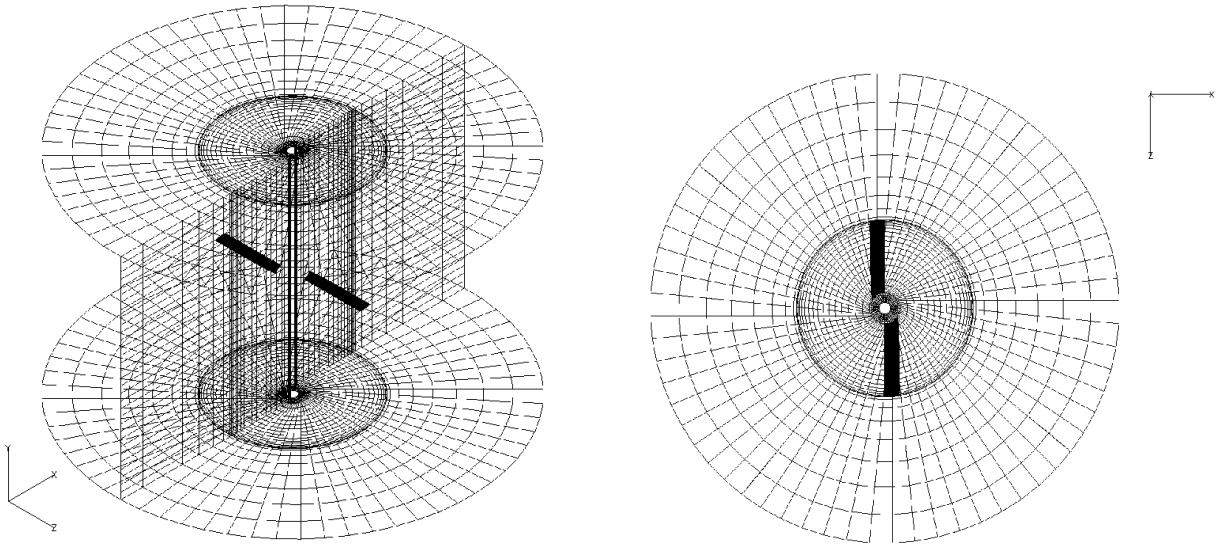

(a) Isometric view (b) Top view

Figure 6. $128 \times 48 \times 32$ **computational mesh cells per blade modeling an untwisted, untapered, two-bladed NACA 0012 rotor with an aspect ratio of 7 for the Euler calculation of a rotor in forward flight**

VI.E. Cost Comparison

As a comparison to the traditional backward difference formula,[23] a RANS calculation of a rotor in forward flight for the same case would require the following operations at the minimum:

- 180 time steps per revolution (more likely 360 time steps, if not more).
- 40 multigrid cycles per time step.
- 6 complete cycles to establish periodicity of the flow field.

This means at least 43200 cycles would be required to solve the same problem, whereas the calculation with the Time Spectral method used only 500 multigrid cycles. Therefore the Time Spectral method is at least two orders of magnitude faster than the backward difference formula.

VII. Computed Results with Vorticity Confinement

THE test case was a fully compressible Euler computation of wing tip vortex of a NACA 0012 wing with an aspect ratio of 3. The free stream Mach number was 0.8 and the angle of attack was 5 degrees. At $z = 0$, a symmetry plane boundary condition was used. Riemann invariants boundary condition was applied at the far-field and a flow tangency boundary condition was used on the wing. The formulation of the Vorticity Confinement method was taken from Eq. (21). Calculations were performed with four different values of the confinement parameter ϵ.

The mesh was generated internally by the flow solver and was a typical C-mesh type with $160 \times 32 \times 48$ mesh cells with 32 cells on the wing. The reference chord length was unity and the trailing edge was located at $x = 1$. The coefficient ϵ was fixed at 0, 0.025, 0.05, and 0.075. The results from the calculations are shown in Fig. 10. There are four cut-planes normal to the x direction located at $x = 2, 4, 6$, and 8, where the vorticity magnitude was plotted. One can observe that the vortex structure was still quite well maintained even after eight chord lengths away with the confinement term. The effectiveness of this depended on the strength of the confinement parameter. For the case of no confinement $\epsilon = 0$, the vorticity dissipated very quickly.

Figure 11 shows the distribution of the coefficient of pressure on the wing at three different span stations. The effect of adding the confinement term was negligible and the distribution of the coefficient of pressure

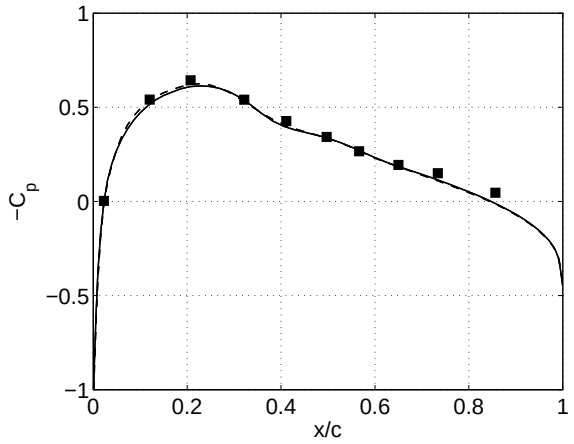

(a) C_p distribution at $\psi = 30°$

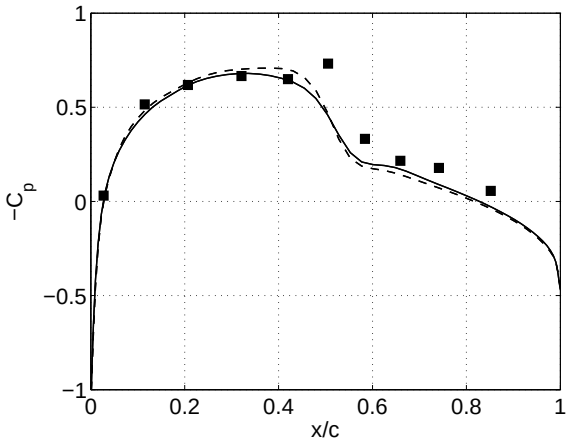

(b) C_p distribution at $\psi = 60°$

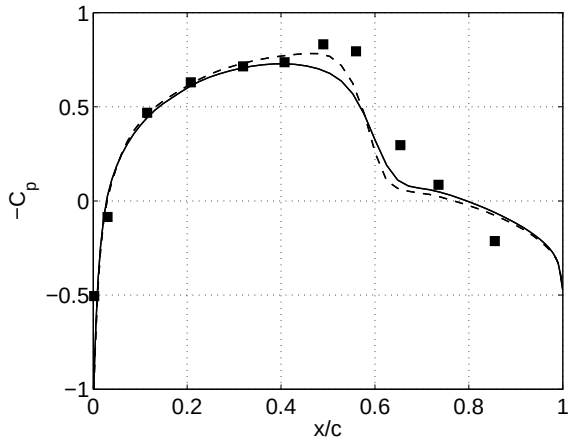

(c) C_p distribution at $\psi = 90°$

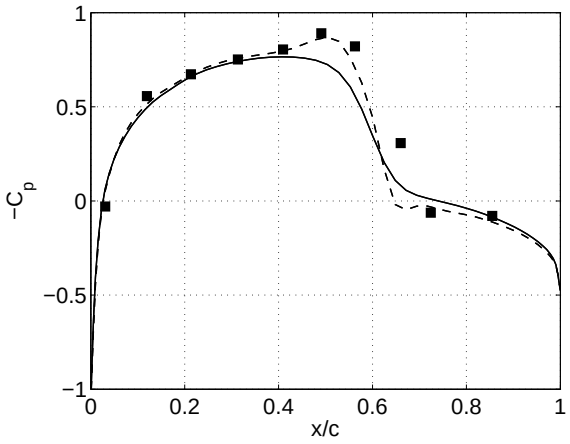

(d) C_p distribution at $\psi = 120°$

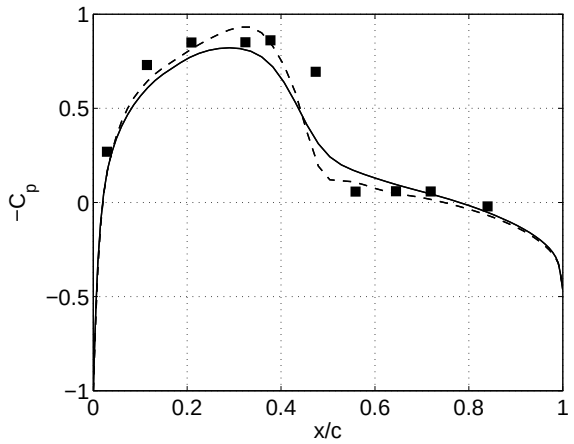

(e) C_p distribution at $\psi = 150°$

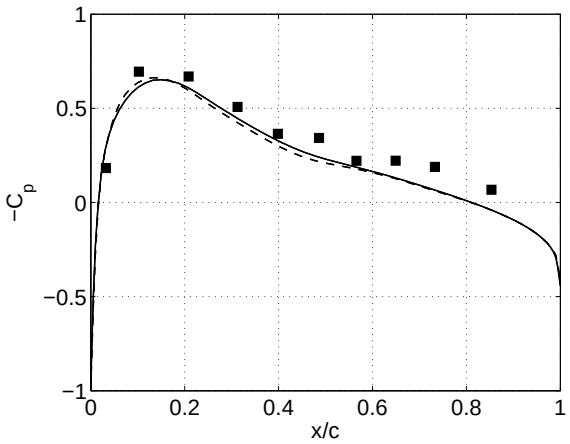

(f) C_p distribution at $\psi = 180°$

Figure 7. Coefficient of pressure distribution on a blade section at $r/R = 0.893$ on a nonlifting rotor in forward flight from Euler calculations, $M_{tip} = 0.8$, $\theta_c = 0°$, $\mu = 0.2$, $N = 12$: ■ denotes the experimental values of C_p, — denotes the result using the JST dissipation scheme, and − − denotes the result using the CUSP dissipation scheme.

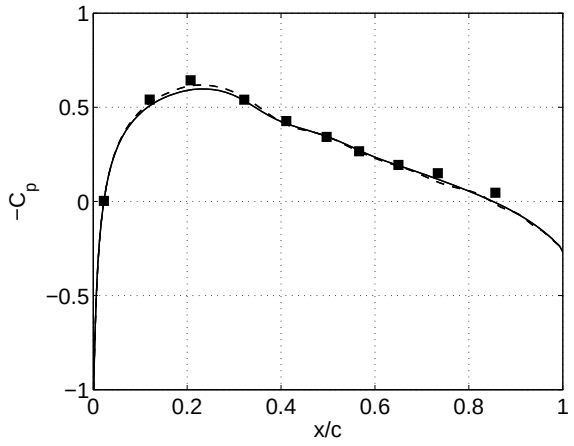

(a) C_p distribution at $\psi = 30°$

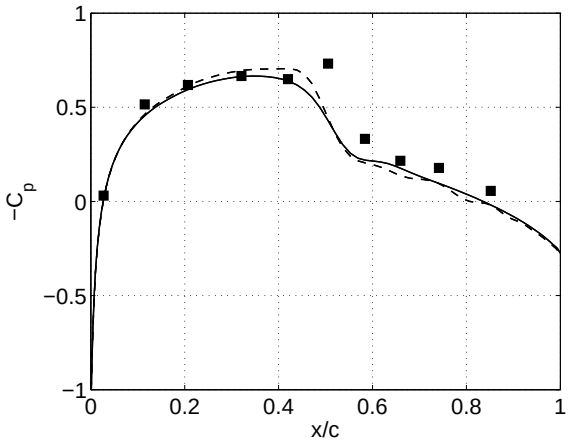

(b) C_p distribution at $\psi = 60°$

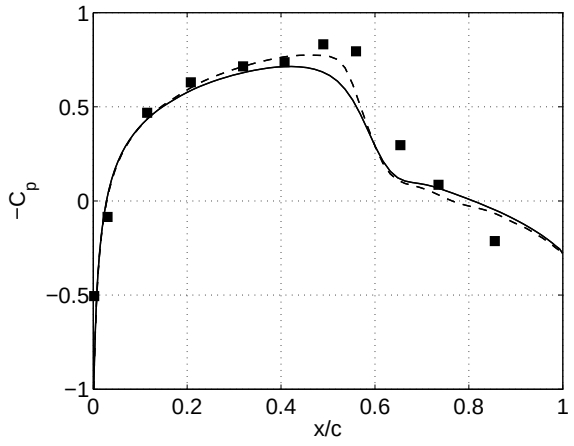

(c) C_p distribution at $\psi = 90°$

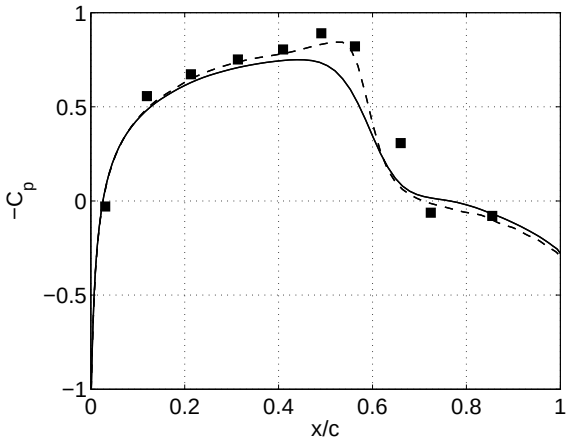

(d) C_p distribution at $\psi = 120°$

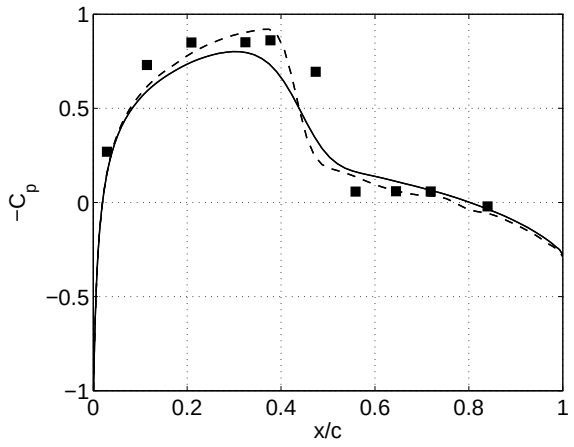

(e) C_p distribution at $\psi = 150°$

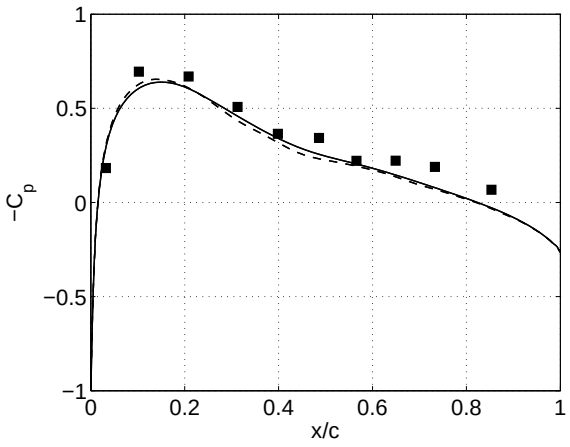

(f) C_p distribution at $\psi = 180°$

Figure 8. Coefficient of pressure distribution on a blade section at $r/R = 0.893$ on a nonlifting rotor in forward flight from RANS calculations, $\mathbf{M_{tip} = 0.8}$, $\theta_c = 0°$, $\mu = 0.2$, $N = 12$: ■ denotes the experimental values of C_p, — denotes the result using the JST dissipation scheme, and − − denotes the result using the CUSP dissipation scheme.

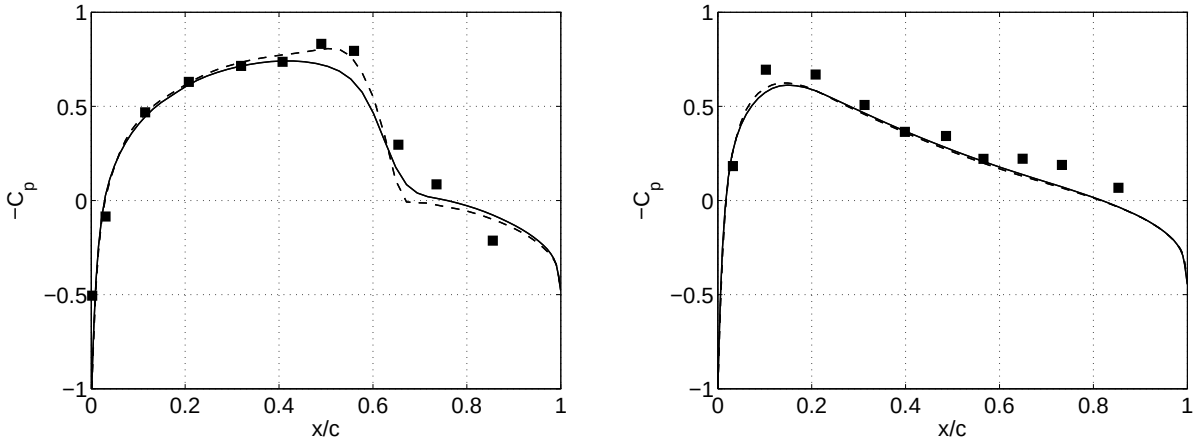

(a) C_p distribution at $\psi = 90°$

(b) C_p distribution at $\psi = 180°$

Figure 9. Coefficient of pressure distribution on a blade section at $r/R = 0.893$ on a nonlifting rotor in forward flight from Euler calculations, $N = 4$, $\mathbf{M_{tip} = 0.8}$, $\theta_c = 0°$, $\mu = 0.2$: ■ denotes the experimental values of C_p, — denotes the result using the JST dissipation scheme, and − − denotes the result using the CUSP dissipation scheme.

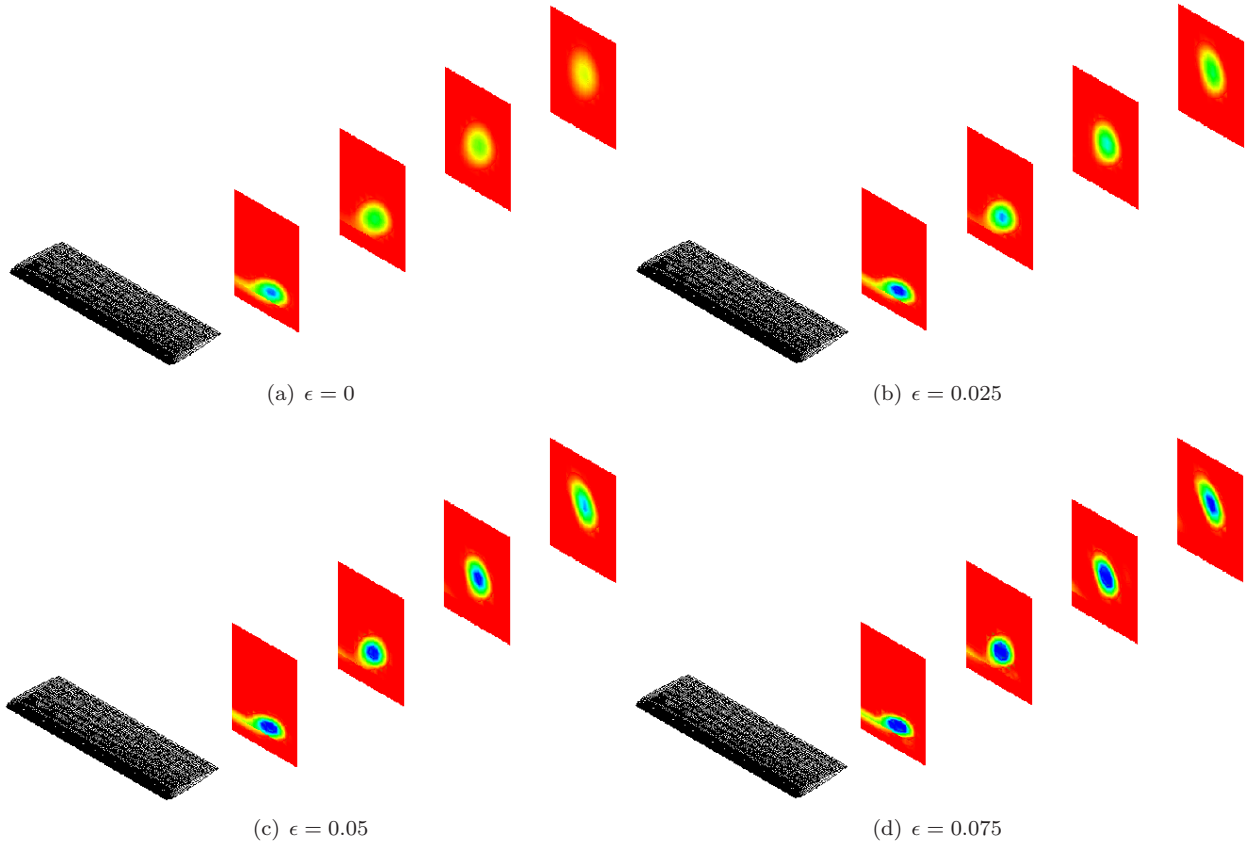

(a) $\epsilon = 0$

(b) $\epsilon = 0.025$

(c) $\epsilon = 0.05$

(d) $\epsilon = 0.075$

Figure 10. Vorticity magnitude on NACA 0012 wing for different values of ϵ: $M_\infty = 0.8$, $\alpha = 5$, aspect ratio = 3.

for each value of ϵ collapsed into one line. The coefficients of lift and drag at three different span stations are listed in Table 1 and are plotted separately in Fig. 12. The coefficients of lift and drag decreased by approximately 0.3% and 0.5% respectively as the confinement parameter ϵ increased from zero to 0.075 at $z = 0.891$, and up to 1.3% for both coefficients at $z = 2.766$. The location $z = 2.766$ was very close to

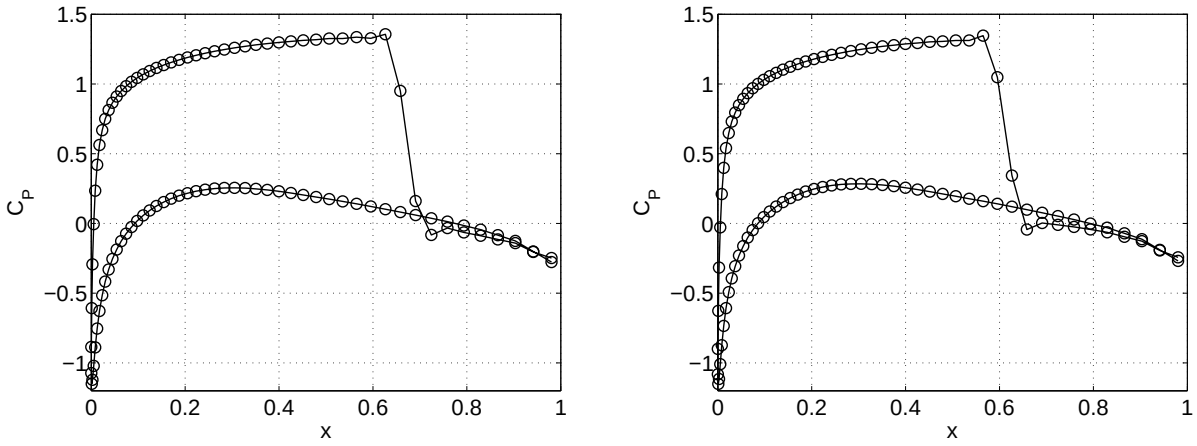

(a) Span station $z = 0.891$

(b) Span station $z = 1.828$

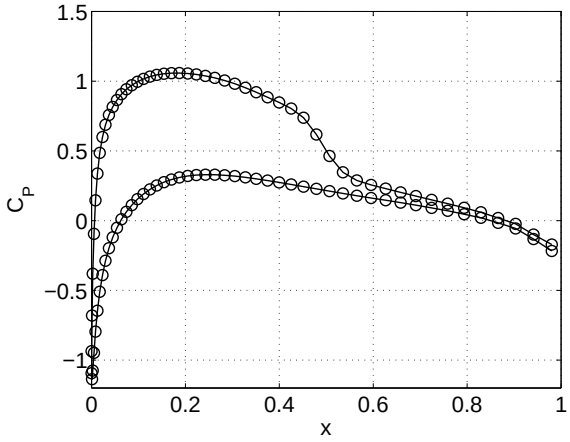

(c) Span station $z = 2.766$

Figure 11. Coefficient of pressure distribution at three span stations on NACA 0012 wing for four different values of ϵ: — ∘ — denotes $\epsilon = 0$, $\cdots$ denotes $\epsilon = 0.025$, $- \cdot -$ denotes $\epsilon = 0.05$, $- -$ denotes $\epsilon = 0.075$, $\mathbf{M}_\infty = 0.8$, $\alpha = 5$, aspect ratio = 3.

	$z = 0.891$		$z = 1.828$		$z = 2.766$	
ϵ	c_l	c_d	c_l	c_d	c_l	c_d
0	0.7098	0.0792	0.6123	0.0651	0.3869	0.0394
0.025	0.7091	0.0791	0.6114	0.0650	0.3851	0.0393
0.050	0.7083	0.0790	0.6103	0.0649	0.3833	0.0391
0.075	0.7074	0.0788	0.6093	0.0647	0.3817	0.0389

Table 1. Coefficients of lift and drag from Euler calculation of a NACA 0012 wing for different values of ϵ at three different span stations: $\mathbf{M}_\infty = 0.8$, $\alpha = 5$, aspect ratio = 3.

the tip of the wing ($z_{\text{tip}} = 3$), and this was where the tip vortex was generated. Therefore the difference in both c_l and c_d for different values of the confinement parameter was expected to be the largest at this location. The results from this test case indicate that the new formulation works well for transonic flow calculation and that the inclusion of the confinement term does not diminish the ability of the flow solver to capture discontinuity. The implementation of the new formulation of Vorticity Confinement is currently

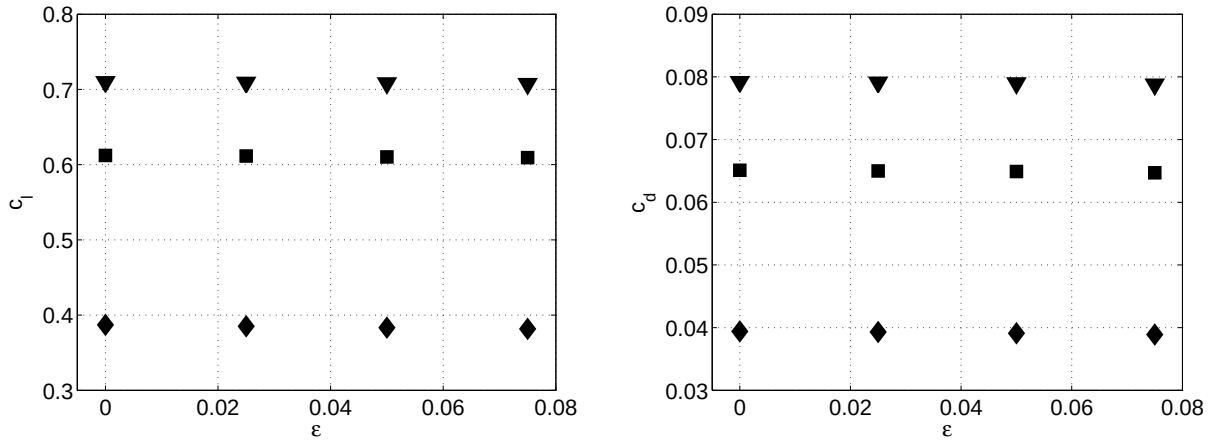

(a) Section c_l (b) Section c_d

Figure 12. Coefficients of lift and drag at three span stations from Euler calculation of a NACA 0012 wing for four different values of ϵ: ▼ at the span station $z = 0.891$, ■ at the span station $z = 1.828$, ♦ at the span station $z = 2.766$, $M_\infty = 0.8$, $\alpha = 5$, aspect ratio = 3.

under investigation for rotorcraft flow.

VIII. Summary & Conclusion

It has been shown that the Time Spectral method is capable of accurately predicting the helicopter aerodynamics. The method is at least two orders of magnitude cheaper than the traditional implicit dual time stepping scheme, and is simpler to implement compared to the nonlinear frequency domain technique. Even when only four time instances were used in forward flight calculations, the flow solver was still able to predict the distribution of the coefficient of pressure accurately. The new formulation of the Vorticity Confinement method needs further investigation and validation before becoming robust enough for rotorcraft flow computation but the new formulation looks promising as it has no effect on the surface pressure distribution and only up to 1.3% error in the values of the coefficients of lift and drag. Additionally, the parameter ϵ is now a true dimensionless parameter and the calculation of a helicity reflects the direction of the vortical structures of the rotorcraft flow field.

References

[1]Jameson, A., Schmidt, W., and Turkel, E., "Numerical Solutions of the Euler Equations by Finite Volume Methods Using Runge–Kutta Time-Stepping Schemes," *AIAA 14th Fluid and Plasma Conference*, Palo Alto, CA, June 1981, AIAA Paper 1981–1259.

[2]Jameson, A., "Analysis and Design of Numerical Schemes for Gas Dynamics 1: Artificial Diffusion, Upwind Biasing, Limiters and Their Effect on Accuracy and Multigrid Convergence," *International Journal of Computational Fluid Dynamics*, Vol. 4, 1995, pp. 171–218.

[3]Jameson, A., "Analysis and Design of Numerical Schemes for Gas Dynamics 2: Artificial Diffusion and Discrete Shock Structure," *International Journal of Computational Fluid Dynamics*, Vol. 5, 1995, pp. 1–38.

[4]Sheffer, S. G., Alonso, J. J., Martinelli, L., and Jameson, A., "Time-Accurate Simulation of Helicopter Rotor Flows Including Aeroelastic Effects," *AIAA 35th Aerospace Sciences Meeting & Exhibit*, Reno, NV, January 1997, AIAA Paper 1997–0399.

[5]Caradonna, F. X. and Isom, M. P., "Subsonic and Transonic Potential Flow over Helicopter Rotor Blades," *AIAA Journal*, Vol. 10, No. 12, 1972, pp. 1606–1612.

[6]Caradonna, F. X. and Isom, M. P., "Numerical Calculation of Unsteady Transonic Potential Flow over Helicopter Rotor Blades," *AIAA Journal*, Vol. 14, No. 4, 1976, pp. 482–488.

[7]Caradonna, F. X. and Philippe, J. J., "The Flow Over a Helicopter Blade Tip in the Transonic Regime," *Vertica*, Vol. 2, 1978, pp. 43–60.

[8]Agarwal, R. K. and Deese, J. E., "Euler Calculations for Flowfield of a Helicopter Rotor in Hover," *Journal of Aircraft*, Vol. 24, No. 4, April 1987, pp. 231–238.

[9]Agarwal, R. K. and Deese, J. E., "Navier–Stokes Calculations of the Flowfield of a Helicopter Rotor in Hover," *AIAA 26th Aerospace Sciences Meeting & Exhibit*, Reno, NV, January 1988, AIAA Paper 1988–0106.

[10]Srinivasan, G. R., Raghavan, V., and Duque, E. P. N., "Flowfield Analysis of Modern Helicopter Rotors in Hover by Navier–Stokes Method," *AHS and Royal Aeronautical Society, Technical Specialists' Meeting on Rotorcraft Acoustics/Fluid Dynamics Proceedings*, Philadelphia, PA, October 1991.

[11]Srinivasan, G. R., Baeder, J. D., Obayashi, S., and McCroskey, W. J., "Flowfield of a Lifting Rotor in Hover: A Navier–Stokes Simulation," *AIAA Journal*, Vol. 30, No. 10, October 1992.

[12]Allen, C. B., "Numerical Simulation of Multi-Bladed Rotors in Lifting Forward Flight," *AIAA 21st Applied Aerodynamics Conference*, Orlando, FL, June 2003, AIAA Paper 2003–4080.

[13]Allen, C. B., "Multi-Bladed lifting Rotor Simulation in Hover, Forward Flight, and Ground Effect," *AIAA 22nd Applied Aerodynamics Conference*, Providence, RI, August 2004, AIAA Paper 2004–5288.

[14]Allen, C. B., "An Unsteady Multiblock Multigrid Scheme for Lifting Forward Flight Rotor Simulation," *International Journal for Numerical Methods in Fluids*, Vol. 45, No. 9, 2004, pp. 973–984.

[15]Allen, C. B., "Parallel Flow-Solver and Mesh Motion Scheme for Forward Flight Rotor Simulation," *AIAA 24th Applied Aerodynamics Conference*, San Francisco, CA, June 2006, AIAA Paper 2006–3476.

[16]Allen, C. B., "Parallel Simulation of Lifting Rotor Wakes in Forward Flight," *International Journal of Numerical Analysis and Modeling*, Vol. 4, No. 1, 2007, pp. 1–15.

[17]Pomin, H. and Wagner, S., "Navier–Stokes Analysis of Helicopter Rotor Aerodynamics in Hover and Forward Flight," *Journal of Aircraft*, Vol. 39, No. 5, September–October 2002, pp. 813–821, Presented as Paper 2001–0998 at the AIAA 39th Aerospace Sciences Meeting & Exhibit, Reno, NV, January 2001.

[18]Pomin, H. and Wagner, S., "Aeroelastic Analysis of Helicopter Rotor Blades on Deformable Chimera Grids," *AIAA 40th Aerospace Sciences Meeting & Exhibit*, Reno, NV, January 2002, AIAA Paper 2002–0951.

[19]Pomin, H. and Wagner, S., "Aeroelastic Analysis of Helicopter Rotor Blades on Deformable Chimera Grids," *Journal of Aircraft*, Vol. 41, No. 3, September–October 2004, pp. 577–584.

[20]Hassan, A. A., Tung, C., and Sankar, L. N., "Euler Solutions for Self-Generated Rotor Blade–Vortex Interactions," *International Journal for Numerical Methods in Fluids*, Vol. 15, 1992, pp. 427–451, Presented as AIAA paper 1990–1588 at the AIAA 20th Fluids, Plasma Dynamics Conference, Buffalo, New York, June 1990.

[21]Bhagwat, M., Moulton, M. A., and Caradonna, F. X., "Development of a New Potential Flow Based Model for Hover Performace Prediction," *AIAA 43rd Aerospace Sciences Meeting & Exhibit*, Reno, NV, January 2005, AIAA Paper 2005–1367.

[22]Bhagwat, M., Moulton, M. A., and Caradonna, F. X., "Hybrid CFD for Rotor Hover Performance Prediction," *AIAA 24rd Applied Aerodynamics Conference*, San Francisco, CA, June 2006, AIAA Paper 2006–3474.

[23]Jameson, A., "Time Dependent Calculations Using Multigrid, with Applications to Unsteady Flows Past Airfoils and Wings," *AIAA 10th Computational Fluid Dynamics Conference*, Honolulu, HI, July 1991, AIAA Paper 1991–1596.

[24]Gopinath, A. K. and Jameson, A., "Time Spectral Method for Periodic Unsteady Computations over Two- and Three-Dimensional Bodies," *AIAA 43th Aerospace Sciences Meeting & Exhibit*, Reno, NV, January 2005, AIAA Paper 2005–1220.

[25]Hsu, J. and Jameson, A., "An Implicit–Explicit Hybrid Scheme for Calculating Complex Unsteady Flows," *AIAA 40th Aerospace Sciences Meeting & Exhibit*, Reno, NV, January 2002, AIAA Paper 2002–0152.

[26]Hall, K. C., Thomas, J. P., and Clark, W. S., "Computation of Unsteady Nonlinear Flows in Cascades Using a Harmonic Balance Technique," *AIAA Journal*, Vol. 40, No. 5, May 2002.

[27]McMullen, M. S., Jameson, A., and Alonso, J. J., "Acceleration of Convergence to a Periodic Steady State in Turbomachinery Flows," *AIAA 39th Aerospace Sciences Meeting & Exhibit*, Reno, NV, January 2001, AIAA Paper 2001–0152.

[28]McMullen, M. S., Jameson, A., and Alonso, J. J., "Application of a Non-Linear Frequency Domain Solver to the Euler and Navier–Stokes Equations," *AIAA 40th Aerospace Sciences Meeting & Exhibit*, Reno, NV, January 2002, AIAA Paper 2002–0120.

[29]McMullen, M. S., Jameson, A., and Alonso, J. J., "Demonstration of Nonlinear Frequency Domain Methods," *AIAA Journal*, Vol. 44, No. 7, July 2006.

[30]Steinhoff, J., *Frontiers of Computational Fluid Dynamics*, chap. 14 Vorticity Confinement: A New Technique for Computing Vortex Dominated Flows, John Wiley & Sons, 1994, pp. 235–263, eds. Caughey, D. A. & Hafez, M. M.

[31]Steinhoff, J. and Underhill, D., "Modification of Euler Equations for "Vorticity Confinement" – Application to the Computation of Interacting Vortex Rings," *Physics of Fluids*, Vol. 6, No. 8, 1994, pp. 2738–2744.

[32]Hu, G., Grossman, B., and J., S., "Numerical Method for Vorticity Confinement in Compressible Flow," *AIAA Journal*, Vol. 40, No. 10, 2002, pp. 1945–1953.

[33]Hu, G. and Grossman, B., "The Computational of Massively Separated Flows Using Compressible Vorticity Confinement Methods," *AIAA 40th Aerospace Sciences Meeting & Exhibit*, Reno, NV, January 2002, AIAA Paper 2002–0714.

[34]Dadone A., Hu, G. and Grossman, B., "Towards a Better Understanding of Vorticity Confinement Methods in Compressible Flow," *AIAA 15th Computational Fluid Dynamics Conference*, Anaheim, CA, June 2001, AIAA Paper 2001–2639.

[35]Fedkiw, R., Stam, J., and Jensen, H. W., "Visual Simulation of Smoke," *International Conference on Computer Graphics and Interactive Techniques, Proceedings of the 28th Annual Conference on Computer Graphics and Interactive Techniques*, 2001, pp. 15–22.

[36]Löhner, R. and Yang, C., "Vorticity Confinement on Unstructured Grids," *AIAA 40th Aerospace Sciences Meeting & Exhibit*, Reno, NV, January 2002, AIAA Paper 2002–0137.

[37]Löhner, R., Yang, C., and Roger, R., "Tracking Vortices over Large Distances Using Vorticity Confinement," *24th Symposium on Naval Aerodynamics*, Fukuoka, Japan, July 2002.

[38]Baldwin, B. and Lomax, H., "Thin-Layer Approximation and Algebraic Model for Separated Turbulent Flows," *AIAA 16th Aerospace Sciences Meeting*, Huntsville, AL, January 1978, AIAA Paper 1978–0257.

[39]Holmes, D. G. and Tong, S. S., "A Three-Dimensional Euler Solver for Turbomachinery Blade Rows," *American Society of Mechanical Engineers, International Gas Turbine Conference and Exhibit*, Amsterdam, The Netherlands, June 1984.

[40]Canuto, C., Hussaini, M. Y., Quarteroni, A., and Zang, T. A., *Spectral Methods: Evolution to Complex Geometries and Applications to Fluid Dynamics*, Springer–Verlag New York, LLC, 1st ed., September 2007.

[41]Jameson, A., *Numerical Methods in Fluid Dynamics*, Vol. 1127/1985 of *Lecture Notes in Mathematics*, chap. Transonic Flow Calculations, Springer Berlin/Heidelberg, 1985, pp. 156–242, Princeton University MAE Report 1651, March 1984.

[42]Jameson, A., "Solution of the Euler Equations For Two Dimensional Transonic by a Multigrid Method," *Applied Mathematics and Computation*, Vol. 13, 1983, pp. 327–356.

[43]Jameson, A., *Multigrid Methods II*, Vol. 1228 of *Lecture Notes in Mathematics*, chap. Multigrid Algorithms for Compressible Flow Calculations, Springer Berlin/Heidelberg, 1986, pp. 166–201, Proceedings of the 2nd European Conference on Multigrid Methods, Cologne, October 1985.

[44]Robinson, M., "Application of Vorticity Confinement to Inviscid Missile Force and Moment Prediction," *AIAA 42nd Aerospace Sciences Meeting & Exhibit*, Reno, NV, January 2004, AIAA Paper 2004–0717.

[45]Caradonna, F. X. and Tung, C., "Experimental and Analytical Studies of a Model Helicopter Rotor in Hover," Tech. Rep. NASA Technical Memorandum 81232, National Aeronautics and Space Administration, September 1981.

[46]Leishman, J. G., *Principles of Helicopter Aerodynamics*, Cambridge University Press, 2nd ed., April 2006.

[47]Caradonna, F. X., Laub, G. H., and Tung, C., "An Experimental Investigation of the Parallel Blade–Vortex Interaction," Tech. Rep. NASA Technical Memorandum 86005, National Aeronautics and Space Administration, November 1984.